Two ('plus one')-Dimensional Simulation of Pellet Cloud Evolution in the Poloidal Plane Part I: Prescribed Particle Source Strength

P.J. Lalousis [1], L.L. Lengyel*, and R. Schneider

Max-Planck-Institut für Plasmaphysik, EURATOM Association,
Wendelsteinstr, 1, 17491 Greifswald, Germany
[1] Institute for Electronic Structure and Laser, FORTH,
Association EURATOM-Hellenic Republic, Heraklion, Greece

Abstract. The evolution of pellet clouds in magnetically confined thermonuclear plasmas is studied by means of a time-dependent two-dimensional resistive MHD model applicable to the poloidal plane of a plasma torus. A massive neutral particle source representing a pellet traverses the plasma and continuously releases cold and unionized particles. Its motion is confined to a poloidal plane, which is thus considered to be a symmetry plane of the model.
The conservation equations supplemented by Maxwell's equations, Ohm's generalized law, and a number of rate equations are solved for the symmetry plane. To each mesh point of the Eulerian grid in the poloidal plane, a toroidal 'flux tube' is attached. The field-aligned expansion of the ablated substance in these flux tubes and the corresponding change of the state parameters are computed in a Lagrangian approximation. Hence the two-dimensional Eulerian resistive MHD code is operated alternating with the one-dimensional Lagrangian routine.
In the first series of computations, the neutral particle source strength is a prescribed input parameter, the applied magnetic field as well as the initial state parameters of the background plasma are uniform. Results of these calculations are presented and the solutions obtained are discussed.

1. Introduction

A pellet injected into a magnetic confinement machine usually traverses a sequence of nested magnetic flux surfaces. The cold particles released by the pellet form a high-density neutral cloud around it, which rapidly expands. The ablated particles may move both in the poloidal plane and in the toroidal direction. The overall process is thus basically three-dimensional. Typical initial neutral particle velocities are an order of magnitude higher than the pellet injection velocity. The expanding cloud is heated by the incident plasma particles and becomes ionized within some μs.

The ionized particles interact with the magnetic field, their motion across the magnetic field becomes decelerated and, in the absence of drifts, they become confined to

*formerly with Max-Planck-Institut für Plasmaphysik, Garching

magnetic flux tubes whose initial radii are approximately equal to the local ionization radii. For pellets used in up-to-date machines, the ionization radius is an order of magnitude larger than the pellet radius.
The pellet thus moves in its own ablated substance in the direction of the ionized and confined frontal peripheral layer. However, ablation is a self-regulating process: upon approaching the high-temperature peripheral layer the pellet releases an increased number of neutral particles thus reducing the local temperature. If this cooling is sufficiently intense, the pellet moves in a medium of quasi-constant temperature, and the ablation process may be considered to be quasi-steady. In the opposite case, when the cooling effect is insufficient, the pellet traverses layers of alternating higher and lower temperatures and the ablation rate too may become modulated. The characteristic length of this modulation is thus given by the size of the confining flux tube (e.g. ionization radius). The confined ablatant, which shields the pellet from the incident plasma particles, expands freely in the flux tubes along the magnetic field lines. The density line integral $\int ndz$, taken along the field lines piercing the pellet and the shielding cloud surrounding it, is a measure of the effectiveness of collisional shielding against incident plasma particles confined to the same field lines.

In earlier studies, the effect of magnetic fields on the evolution of the pellet cloud and the ablation process had been ignored (neutral gas shielding ablation models, see, for example, [1, 2] or the review [3]). In the next generation of the ablation models, the confinement of the energy carriers and the ablated substance to magnetic flux tubes was taken into account [3 to 9]. The correct definition of the confinement radius required the application of properly posed resistive MHD models [7,8,9]. A comprehensive analysis of pellet injection phenomena, including the existing pellet ablation models, can be found in a recent PPCF topical (pellet) review paper [10].
If $\mathbf{E}\times\mathbf{B}$ - or ∇B-induced drift is present in the plasma (see [11] to [16]), the ablated substance drifts across the magnetic field and the relative position of the pellet to its shielding cloud is independent of the ionization radius. In this case, the local ablation rate may become decoupled from the flux tube parameters of the background plasma. However, drift is a transient phenomenon [17], its duration depends on the evolution of the equilibrating currents in the system considered.

In the absence of drift, the local confinement of the ablated substance to discrete B-aligned flux tubes suggests pellet path discretization in terms of the local confinement radii and the associated flux tube sizes. Such an approach yields, in combination with the self-consistent calculation of the cloud expansion characteristics along the magnetic field lines, pellet penetration depths and/or radiation characteristics [8,9] that are in agreement with experimental observations.
Nevertheless, using the flux tube size for discretization imposes a periodicity on the system that may not always reflect physical reality. This is the case, for example, for large pellets producing an abundance of cold particles over the whole pellet path, or in the presence of non-ignorable drift of the ablated substance. In such cases, persuasive information on the evolution of the pellet cloud and the associated ablation

rate history can only be expected from computational models in which *no conditions resembling periodicity or any other prescribed structure* are imposed. For this reason, it was decided to apply a two-dimensional numerical model without taking refuge to the ionization radius as characteristic length of the problem. The model was developed originally for computing two-dimensional current- and field distributions in MHD flows with nonequilibrium ionization [18]. Here the model is applied for calculating analogous distributions in the poloidal plane. The effect of the third dimension (e.g. plasma dynamic processes along the field lines) is also taken into account. The basic characteristics of this '2+1'-dimensional model were presented in [19] in which the drift of a carbon plasma cloud over a vaporizing divertor plate following a disruption event was computed. Further results of preliminary nature are given in [20].
Although the assumption of constant particle source strength and uniform initial background plasma/magnetic field distributions used in this part of the analysis is far from realistic, it allows for a reliability check of the complex 2-dimensional code involved. Furthermore, even in this approximation some relevant information is obtained on a number of pellet-plasma interaction phenomena: the form and size of the partially ionized and radiating region in the wake of the pellet, the characteristic transient times associated with wake formation, the resulting temperature and density patterns around the pellet, and the conditions for the existence of shocks and the magnitude of the the eventual shock heating of the background plasma.
Some of the data obtained, e.g. the radiation patterns, can be compared with experimental observations.

In the second part of the analysis (yet to be done), the 2-dimensional code will be supplemented by a self-consistent ablation model. A prerequisite for applying the ablation model selected is the correct determination of the plasma expansion dynamics and the resulting particle and energy fluxes along the magnetic field lines. For this purpose, a multi-cell Lagrangian routine shall be attached to each mesh point of the poloidal plane. Variable cell number (with cell splitting or new cell generation [7, 9]) shall be applied.
Thus the analysis of arbitrary experimental pellet scenarios shall become possible by prescribing the corresponding boundary conditions and initial plasma parameter distributions. Valuable information can then be obtained on various relevant pellet-plasma interaction phenomena such as the cause of the B-parallel striations occasionally seen in pellet-fuelled discharges and the characteristics of the ∇B-induced drift motion of the ablated pellet substance in particular.

2. Physical Model

The set of equations consisting of the magnetohydrodynamic conservation equations, Maxwell's equations, Ohm's generalized law, and supplemented by rate equations for particle collisions and equations for transport processes (thermal conduction, etc., see

[9] and [19]) is as follows:

$$
\begin{aligned}
&\frac{\partial \rho}{\partial t} \;+\; \nabla \cdot (\rho \mathbf{v}) && = \dot{S}_{abl} \\
&\frac{\partial (\rho \mathbf{v})}{\partial t} \;+\; \nabla \cdot (\rho \mathbf{v}\mathbf{v} \;+\; \mathbf{I}p) && = \mathbf{j} \times \mathbf{B} \\
&\frac{\partial \epsilon}{\partial t} \;+\; \nabla \cdot ((\epsilon + p)\mathbf{v}) && = \mathbf{j} \cdot \mathbf{E} \;- \epsilon_i \dot{n}_e + \;\frac{\dot{S}_{abl}}{m_h} \frac{kT_{pel}}{\gamma - 1} + \;\nabla \cdot (\chi \nabla T) \\
&\nabla \cdot \mathbf{B} && = 0 \\
&\nabla \times \mathbf{B} && = \;\mu_0 \mathbf{j} \\
&\mathbf{j} && = \sigma(\mathbf{E} \;+ \mathbf{v} \times \mathbf{B}) \\
&\frac{\partial n_e}{\partial t} \;+\; \nabla \cdot (n_e \mathbf{v}) && = \dot{n}_e
\end{aligned}
$$

where $\mathbf{v}$ is the macroscopic velocity of the ablated substance and background plasma particles, $\mathbf{I}$p represents the pressure tensor, σ the electrical conductivity (modified Spitzer conductivity, taking also the electron-neutral collisions into account), $\dot{S}_{abl}$ is the particle source strength (ablation rate), and

$$\epsilon \;=\; \frac{p}{(\gamma - 1)} \;+ \frac{1}{2} \rho \mathbf{v} \cdot \mathbf{v}, \qquad \nabla \;\equiv\; (\frac{\partial}{\partial x}, \frac{\partial}{\partial y}).$$

The thermal diffusivity is an ionization-degree-weighted sum of the neutral gas and electron thermal diffusivities: $\chi \;=\; (\alpha - 1)\chi_a + \alpha \chi_e$ ($\chi_i << \chi_e$). Subscripts a, e, i, and h denote atoms, electrons, ions, and heavy particles ($n_h \;=\; n_a \;+\; n_i$), respectively. For the cross-field conduction, anomalous electron conductivity values are used.

The equations are supplemented by the ideal gas state equation:

$$p = nkT.$$

The applied vacuum field is purely toroidal with $R_{tor} \approx \infty$, i.e. helicity effects are, for the time being, neglected.

If a self-consistent description of the scenarios is attempted, the physical processes associated with the toroidal direction such as energy transfer to the pellet and to the ablated pellet substance by energetic plasma particles confined to magnetic field lines, electrostatic shielding, expansion of the ablatant, thermal conduction, etc., must also be taken into account. (The ablation rate is defined by the balance of the energy fluxes at the pellet surface.) Fortunately, these processes are symmetric with respect to the poloidal plane in which the pellet is moving. The poloidal plane can thus be considered as a symmetry plane.

Poloidal currents are induced in the system by the $\mathbf{v} \times \mathbf{B}$ electromotive force (e.g. by its $v_r B_z$ component) and the associated time variation of the magnetic field. These currents are responsible for the B-perp deceleration and confinement of the ionized substance and can be expressed as

$$j_x \;=\; \frac{\partial \psi}{\partial y}, \qquad and \qquad j_y \;=\; -\; \frac{\partial \psi}{\partial x}$$

where ψ represents the 'current stream function' [18] and is proportional to the induced magnetic field:

$$B_z \;=\; B_{z0} \;+\mu_0\psi \;.$$

Taking the curl of Ohm's generalized law and assuming that $\partial/\partial z \equiv 0$, where z denotes the toroidal direction, the z-component of the the curl equation yields a second order partial differential equation for the two-dimensional stream function ψ [18], [19]:

$$\frac{\partial\psi}{\partial t} \;+\; \frac{\partial(v_x\psi)}{\partial x} \;+\; \frac{\partial(v_y\psi)}{\partial y} \quad = \\ \frac{\partial}{\partial x}(\frac{1}{\sigma\mu_0}\frac{\partial\psi}{\partial x}) \;+\; \frac{\partial}{\partial y}(\frac{1}{\sigma\mu_0}\frac{\partial\psi}{\partial y}) \;-\; \frac{1}{\mu_0}\frac{\partial(v_xB_{z0})}{\partial x} \;-\; \frac{1}{\mu_0}\frac{\partial(v_yB_{z0})}{\partial y}$$

Although in the majority of realistic pellet ablation scenarios the inductive part of the current associated with the time variation of the magnetic field is substantially smaller than the $\sigma(\mathbf{v}\times\mathbf{B})$ contribution [21], the equation for ψ is solved here without any further simplifications.

The mathematical treatment of the processes associated with the third dimension requires the solution of the complete set conservation equations for each 'flux tube' attached to the mesh points of the poloidal plane [9]. The analysis of the various processes inherent in these flux tubes requires the application of an adequately large number of Lagrangian fluid cells for each flux tube.

To reduce the associated computational volume and computational time, only a single Lagrangian cell per flux tube is used in the preliminary scenario computations reported here. The energy flux entering into this cell in the B-parallel direction is taken to be equal to the thermal energy flux carried by the background plasma electrons ('free flux limit'). The computed expansion velocities of the Lagrangian cells are, for the time being, sonic-limited.

The Lagrangian description requires the specification of a certain initial physical thickness for the poloidal layer analyzed. The half thickness of this layer h_0 defines the initial length of the Lagrangian cells in the toroidal (z) direction.

In agreement with experimental data concerning the thickness of the radiating layer in the poloidal plane (see, for example, Fig. 2 of [7]), the initial thickness of the first Lagrangian cell attached to the poloidal layer is chosen to be approximately equal to the diameter of the neutral or partially ionized gas sphere surrounding the pellet. This selection corresponds to spherically symmetric expansion of the ablated substance within the ionization time, prior to fully developed MHD interaction. Computational tests showed that deviations of the initial Lagrangian cell lengths from this dimension, within the order of magnitude of the neutral gas cloud diameter, does not notably affect the results.

For the ease of the present preliminary analysis, the applied magnetic field $B_0 \;=\; B_{z0}$, the ablation rate $\dot{S}_{abl}$, the pellet velocity v_p, and the initial temperature and density of the recipient plasma $T_{e0} = T_{i0} = T_0$ and n_{e0} are kept spatially constant in all scenarios described.

3. Numerical Scheme

The mathematical model consists of a system of two-dimensional equations written for the poloidal plane, supplemented by a set of one-dimensional equations which account for the processes associated with the toroidal direction.

Eulerian coordinates with rectangular numerical mesh, uniform or nonuniform, are used for the poloidal plane and a Lagrangian cell system, attached to each element of the Eulerian mesh, for the toroidal direction.

For integrating the equations in time, the system is subdivided in two parts and the equations are solved separately for every time step Δt (in a way similar to the method of fractional steps): (a) solution of the 2-D system of equations for the poloidal plane ('Eulerian step'), followed by (b) the computation of the processes associated with the toroidal direction ('Lagrangian step'). Variable time increment is used for integrating the coupled systems. The constraint on the time step size is determined by the governing system of the 2-D resistive MHD equations.

3.1. Eulerian step

The 2-D system of equations includes time dependent first and second order partial differential equations. The equations are split in two parts: a hyperbolic system and a parabolic one, the last incorporating the temperature- and magnetic field diffusion equations. In the first and second fractional steps, the hyperbolic and parabolic systems are solved separately by applying appropriate solution methods.

In matrix notation, the hyperbolic system is of the structure

$$\frac{\partial \mathbf{U}}{\partial t} + \frac{\partial \mathbf{F}(\mathbf{U})}{\partial x} + \frac{\partial \mathbf{G}(\mathbf{U})}{\partial y} = 0$$

where the vector $\mathbf{U}$ denotes $\mathbf{U} = [\rho, \rho v_x, \rho v_y, \epsilon, B_z, n_e]$.

A finite volume discretization scheme is applied:

$$U_{i,j}^{m+1} = U_{i,j}^{m} + \Delta t \left[\frac{1}{\Delta x}(f_{i+\frac{1}{2},j} - f_{i-\frac{1}{2},j}) + \frac{1}{\Delta y}(g_{i,j+\frac{1}{2}} - g_{i,j-\frac{1}{2}}) \right] \quad ,$$

where U^{m+1} is the time-advanced value of the function U, $f_{i+\frac{1}{2},j}$ and $g_{i,j+\frac{1}{2}}$ are numerical fluxes at the $x_{i+\frac{1}{2}}$ and $y_{j+\frac{1}{2}}$ interfaces of a numerical cell, respectively. The conservative variables are defined at the cell centers, the fluxes are computed at their lateral surfaces.

For computing the numerical fluxes, the Total Variation Diminishing(TVD) Lax-Friedrichs method is applied [22]:

$$f_{i+\frac{1}{2}} = \frac{1}{2} \left[F(U_{i+\frac{1}{2}}^{L}) + F(U_{i+\frac{1}{2}}^{R}) - max(\frac{\lambda^L + \lambda^R}{2})(U_{i+\frac{1}{2}}^{R} - U_{i+\frac{1}{2}}^{L}) \right] \quad ,$$

where $\lambda = v_x + c_s + v_a$, c_s and v_a are the sonic and Alfven velocities respectively;

$$U^L_{i+\frac{1}{2}} = U^m_i + \frac{\overline{\Delta U^m_i}}{2}, \qquad U^R_{i+\frac{1}{2}} = U^m_{i+1} - \frac{\overline{\Delta U^m_{i+1}}}{2} .$$

The superscripts L and R denote the left and right sides of an interface x separating two adjacent numerical cells, the overline terms are computed using the slope limiter minmod method [22]. The numerical fluxes in the y-direction are treated similarly. Since the TVD method is an explicit numerical method, the restriction on the time step is based on the largest characteristic speed, and is

$$\Delta t \leq min(\frac{\Delta x}{2(v_x + c_s + v_a)} , \frac{\Delta y}{2(v_y + c_s + v_a)}).$$

The TVD method is 2nd order accurate in space. No artificial viscosity is used in these computations.

The source terms present in the equations are treated explicitly or by means of a predictor-corrector-type iterative procedure. Having integrated the hyperbolic system over a time increment Δt, central finite differences are used to discretize and implicitly solve the parabolic equations. The corresponding matrix equations are solved iteratively by using the generalized minimal residual method [23].

3.2. Lagrangian step

The 1-D conservation equations, mass, momentum, and pressure are solved for the toroidal direction by applying a standard Lagrangian procedure (see, for example, [9]) to the cells attached to the 2-D poloidal numerical grid. Prior to performing the Lagrangian step, the plasma state parameters are adjusted by accounting for the the effects of volumetric expansion in the z-direction:

$$u^* = \left[V_0 u^E + (V^m - V_0)u^m\right]/V^m ,$$

where u denotes n_h, n_e, or p, respectively. Here $V^m = area \times z(t)$, is a Lagrangian volume element, z(t) is the length of a cell in the toroidal direction at time = t,
and $area = \Delta x \times \Delta y$ is an area element in the poloidal plane. $V_0 = area \times h_0$ is the Lagrangian volume element at time=0, h_0 is the initial cell length in the toroidal direction.
The superscript m denotes values at the old time step (time=t), whereas the superscript E implies values at the end of an Eulerian step $(t + \Delta t)$.
The x and y components of the momentum and the value of the total energy (*kinetic+internal*) are adjusted accordingly.

4. Computational Scenarios

Prior to performing calculations with particle sources traversing the plasma in the poloidal plane, a number of test calculations were performed. The purpose of these calculations was, besides testing the reliability of the numerical scheme and the accuracy of the results obtained, to assist the interpretation of the results obtained in more complex situations.

All test calculations reported in this section were performed by operating the code in two-dimensional ('plus one') mode.

4.1. Plane Shock Wave Test

In the course of scenario calculations, it was noticed that for certain particle source strength - plasma temperature combinations, both being sufficiently high, the resulting 'explosive' expansion of the high-density ablatant cloud may produce weak shock waves penetrating the background plasma. *Due to shock heating, a moderate local elevation of the background plasma temperature was recorded.*

To make certain that the observed effect is physical, shock tests were performed: one half of the domain was filled with an initially high-pressure deuterium plasma (shock tube scenario). The high- and low-pressure domains were separated by a fictitious 'diaphragm' which was ruptured at time = 0. The time evolution of the plasma dynamic parameters both on the high- and low-pressure sides were subsequently computed. Various input parameter combinations were tested by having either high-temperature or low-temperature 'driver gas' on the high-pressure side. (The dissipative processes were not turned off during the numerical computations.)

Shock wave relations applicable to discontinuity surfaces at an ablating pellet surface with phase change and/or local heat sources/sinks present were derived in [24]. As usual, steady state was assumed and the conditions of mass-, momentum-, and energy conservation were applied to the two sides of the discontinuity surface. It was assumed that the degree of ionization at the ablation front is negligibly small and thus the magnetic field strength remains unaffected.

Relatively little is known about the evolution of magnetohydrodynamic shocks in partially ionized gases. The presence of the neutral particle component and the associated ionization- and recombination processes provide an additional degree of freedom for the establishment of the equilibrium plasma state parameters behind the shock wave.

Here we extend the expression obtained in [24] and include possible changes of the ionization state and of the strength of the normal magnetic field component, the only field component we consider in this work, across the discontinuity surface. In the analytical relations derived, dissipative processes are not taken into account.

4.1.1. Generalized shock relations Assuming that mass, momentum and energy are conserved across a shock wave, the expression relating the undisturbed plasma parameters (subscript '0') with those on the downstream side of the discontinuity surface (subscript '1') can be written as follows:

$$\frac{\frac{(1+\alpha_1)}{(1+\alpha_0)}\frac{p_1}{p_0}\frac{\alpha_1-\alpha_0}{1+\alpha_1}\frac{\rho_1}{\rho_0} + \beta_0\left(\frac{B_1}{B_0}-1\right)^3 - 1}{\frac{\gamma+1}{\gamma-1} - \frac{\rho_1}{\rho_0}}$$

where $\alpha = n_e/n_h, \quad n_h = n_a + n_i$, note that $p_{total} = (1+\alpha)n_h kT$.

As before, the subscripts a, i, e, and h denote neutral atoms, ions, electrons, and heavy particles, respectively. The quantity ϵ_i is ionization energy per particle. For a deuterium plasma $2\epsilon_i/\mathrm{k} = 3.67 \times 10^5 K$.

The change of the plasma temperature across the shock wave follows from the ideal gas state equation:

$$T_1/T_0 = (1+\alpha_0)/(1+\alpha_1) * (p_1/p_0)/(\rho_1/\rho_0).$$

In the absence of magnetic fields, ($\beta_0 \equiv 0$), or at negligible magnetic field changes ($B_1/B_0 \approx 1$), the expression relating $\frac{\rho_1}{\rho_0}$ to $\frac{p_1}{p_0}$ can be approximated by

$$\frac{\rho_1}{\rho_0} = \frac{\frac{\gamma+1}{\gamma-1}\frac{1+\alpha_1}{1+\alpha_0}\frac{p_1}{p_0} + 1}{\frac{\gamma+1}{\gamma-1} + \frac{1+\alpha_1}{1+\alpha_0}\frac{p_1}{p_0} - \frac{2\epsilon_i}{kT_0}\frac{\alpha_1-\alpha_0}{1+\alpha_0}}$$

If, in addition, there is no change in the ionization degree (for example shock waves in cold or in fully ionized gases) the above equation reduces to the known Rankine-Hugoniot expression representing an explicit relation between the pressure and density jumps across gasdynamic shock waves (see, for example, [25]).

The change of the magnetic field strength across a shock wave follows from Maxwell's equations:

$$\frac{\partial \mathbf{B}}{\partial t} \;=\; \nabla \times (\mathbf{v} \times \mathbf{B}) \;-\; \nabla \times (\chi_m \nabla \times \mathbf{B})$$

For the vector fields considered and with $\mathbf{v} = \hat{x}v$, $\mathbf{B} = \hat{z}B$

$\partial/\partial t \equiv 0$, $\partial/\partial z \equiv 0$, we have

$$B_z \nabla \cdot \mathbf{v} \;+\; (\mathbf{v} \cdot \nabla) B_z \;=\; \nabla \cdot (\mathbf{v} B_z) \;=\; \nabla \cdot (\chi_m \nabla B_z).$$

Assuming negligible dissipation, i.e. $\chi_m = 0$, we have $B_1 v_1 = B_0 v_0$, i.e.

$$B_1/B_0 = v_0/v_1 = \rho_1/\rho_0$$

The reliability of the numerical procedure can thus be checked by comparing the results to these analytic relations.

4.1.2. Change of the ionization state across a shock wave Figs. 1a to 1d show the evolution of the density, temperature, pressure, and ionization degree distributions for a shock produced in a partially ionized low-temperature plasma in the absence magnetic fields. The initial plasma parameters specified for this case are as follows:

$n_{hL} = 5 \times 10^{23}\ m^{-3},\ T_{0L} = 1.5\ eV,\ n_{hR}/n_{hL} = 0.1,\ T_{0R}/T_{0L} = 1,\ B_0 = 0,$

where subscripts L and R denote initial quantities on the left- and right-hand sides of the virtual diaphragm, respectively. The initial values of the ionization degree on the left- and right-sides of the virtual diaphragm are 0.42 and 0.78 .

The three curves shown in a frame correspond to 10, 15, and 25 μs following the moment of diaphragm rupture. The shock wave propagates from the left to the right.

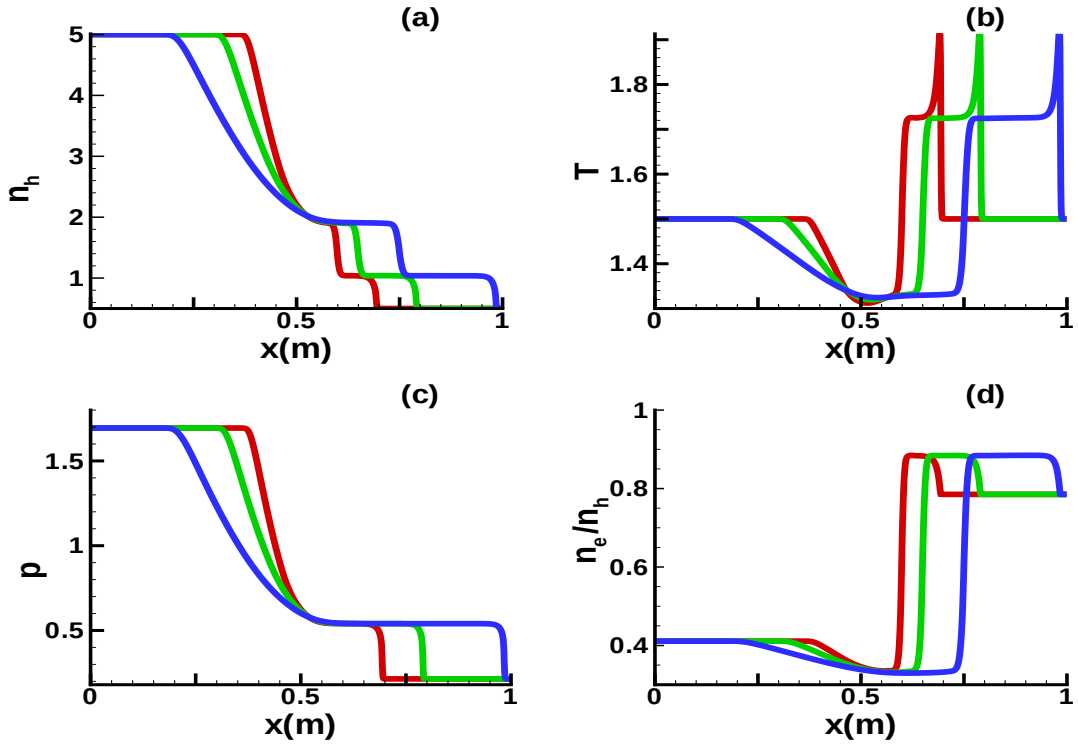

Figure 1. Change of the plasma parameters across a plane ionizing shock wave: (a) heavy particle density ($10^{23} m^{-3}$), (b) temperature (eV), (c) pressure ($10^5 N/m^2$), (d) ionization degree (n_e/n_h).

The curves display the well known characteristics of shock tube regions (see, for example, [25]): the temperature abruptly rises across the moving shock and drops below its initial value at the contact surface (the boundary of the high- and low-pressure substances initially separated by the diaphragm). The velocity and the pressure remain constant across the contact surface and an expansion fan (a train of rarefaction waves) propagates backward into the originally high-pressure region.

The temperature peaks seen at the shock front are of particular interest. They are associated with the finite ionization and recombination rates specified. The temperature

rises practically instantaneously at constant electron density. It decreases subsequently and the electron density rises in accordance with the finite ionization and recombination rates specified. The *peak* temperature value corresponds to frozen-in ionization state and satisfies the generalized shock relation with the ionization term set equal to zero. The *quasi-steady* temperature value following the peak is in agreement with the analytic value corresponding to the presence of the ionization term in the shock relation. In scenarios without ionization/recombination processes (fully ionized substance, cold gas, etc.,) these peaks are absent.

Plasma velocities of the order of 10^4 m/s are generated, the shock wave velocity estimated from the positions of the curves is $\approx 1.8 \times 10^4$ m/s (Mach No ≈ 1.23) at the end of the time interval considered. Comparing the plotted values with the analytical results for the given p_1/p_0 ratio, the deviation is of the order of 1 %.

4.1.3. Change of the magnetic field strength across a shock

Results of another shock scenario calculation, i.e. the evolutions of the heavy particle density, temperature, pressure, and magnetic field distributions, are summarized in Figs. 2a to 2d. The three curves seen correspond to time instants of 0.1, 0.3, and 0.4 μs, respectively. The input data used for this scenario are as follows:

$n_{hL} = 10^{22}\ m^{-3},\ T_{0L} = 1\ keV\ n_{gR}/n_{hL} = 0.1,\ T_{0R}/T_{0L} = 1,\ B_0 = 2\ Tesla.$

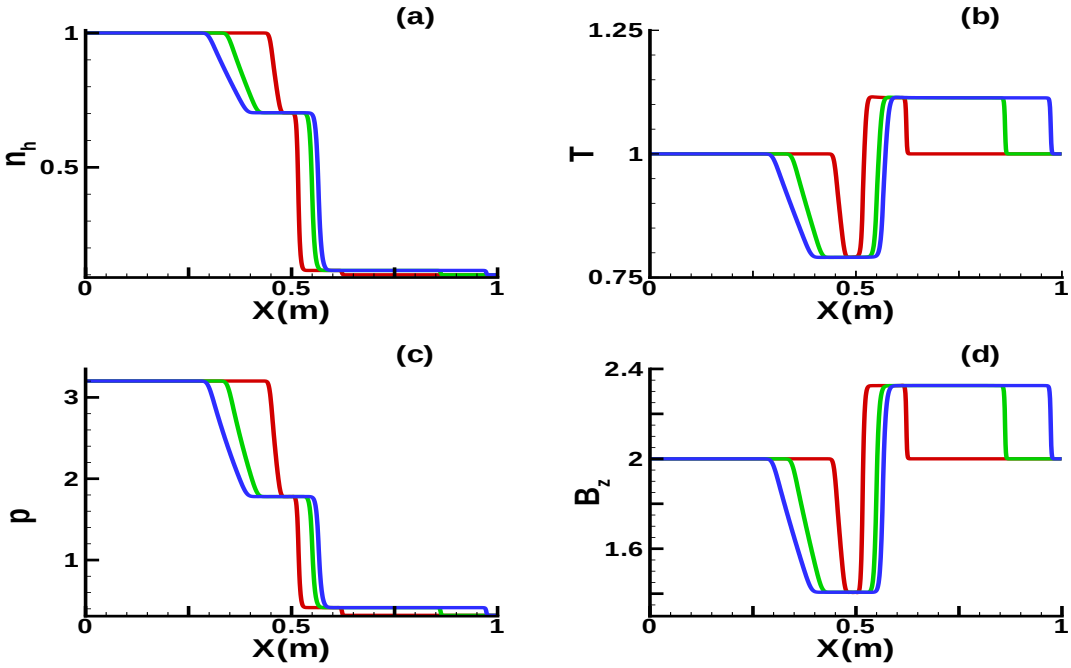

Figure 2. Change of the plasma parameters and the magnetic field strength across a plane MHD shock wave: (a) heavy particle density ($10^{22} m^{-3}$), (b) temperature (keV), (c) pressure ($10^6 N/m^2$), (d) magnetic field strength B_z ($Tesla$). The three curves correspond to three positions of the shock wave propagating from the left to the right.

In this case, the plasma is fully ionized on both sides of the shock wave. Since the plasma temperature is high, quasi-frozen-in field conditions exist. Comparing Figs. 2b and 2d, the correspondence of the the density- and magnetic field strength jumps across the shock wave becomes apparent. In all regions with quasi-frozen-in conditions, the magnetic field changes correspond to the local density changes. The short physical times displayed are associated with the initial conditions (high T_0) chosen. As a result of (total) energy conservation, the local plasma pressure increases on the l.h.s. of the contact surface in the diamagnetic domain where the magnetic field strength decreases and *an intermediate pressure plateau appears*, which is absent if no magnetic field strength change takes place (see Figure 1). The deviation between the analytical and numerical values of the shock wave characteristics is less than 1% for all quantities cited.

4.1.4. Axially symmetric (cylindrical) shock waves

In these scenarios, a high-pressure cylindrical blob of 10 cm diameter was placed in the center of the computational domain. The blob may have been hot or cold. At time = 0 the blob was released and its expansion was computed in the rectangular (x,y) coordinate system (two-dim. computational mode). Figures 3a to 3d correspond to the set of initial blob and background plasma parameters

$n_{bl} = 10^{23}\ m^{-3},\ T_{bl} = \ \ 5\ eV,\ r_{bl} = 5\ cm,\ \ n_{e0} = 10^{20}\ m^{-3},\ T_{e0} = 500\ eV,\ B = 1.5\ Tesla.$

The four curves shown in Figs. 3a and 3b correspond to the time levels of 0.4, 0.8, 1.4, and 1.8 μs, respectively. In the scenario considered, the mass removal, e.g. the velocity in the toroidal direction v_z, was set equal to zero.

The low-temperature partially ionized blob expands until its periphery becomes fully ionized, decelerated, and confined. A part of the kinetic energy is converted into magnetic energy: the field lines become stretched. At the center of the blob, a diamagnetic cavity forms. The confined peripheral layer stops and repels the radially outward moving mass, velocity reversal takes place. The motion becomes a slowly decaying periodic splashing motion with a frequency given by the corresponding Alfven frequency. The case is analogous to some barium clouds release experiments in the magnetosphere.

The confinement radii (some tens of km) and the oscillation frequencies observed in those experiments were successfully reproduced with an early version of the pellet code discussed here (see [26] and the source works cited there).

Figures 3a and 3b show the radial velocity and magnetic field distributions in the expanding blob for four different time instants. As can be seen, the velocity direction reverses approximately every 2nd μs. The magnetic field becomes periodically compressed by the splashing plasma (quasi-frozen-in state), and follows the same oscillation pattern.

If toroidal expansion is admitted (i.e. the Lagrangian routine is turned on), the

oscillation amplitudes become strongly damped. Figures 3c and 3d display the time histories of the pressure maximum monitored in the whole computational domain without (Fig. 3c) and with (Fig. 3d) toroidal expansion admitted. Sonic limit was applied to the outflow velocity. The notable difference between the two cases warrants accurate computation of the toroidal expansion dynamics, which is yet to be done. Also the intensity of the shock waves that may develop in the system strongly depends on the characteristics of the toroidal outflow.

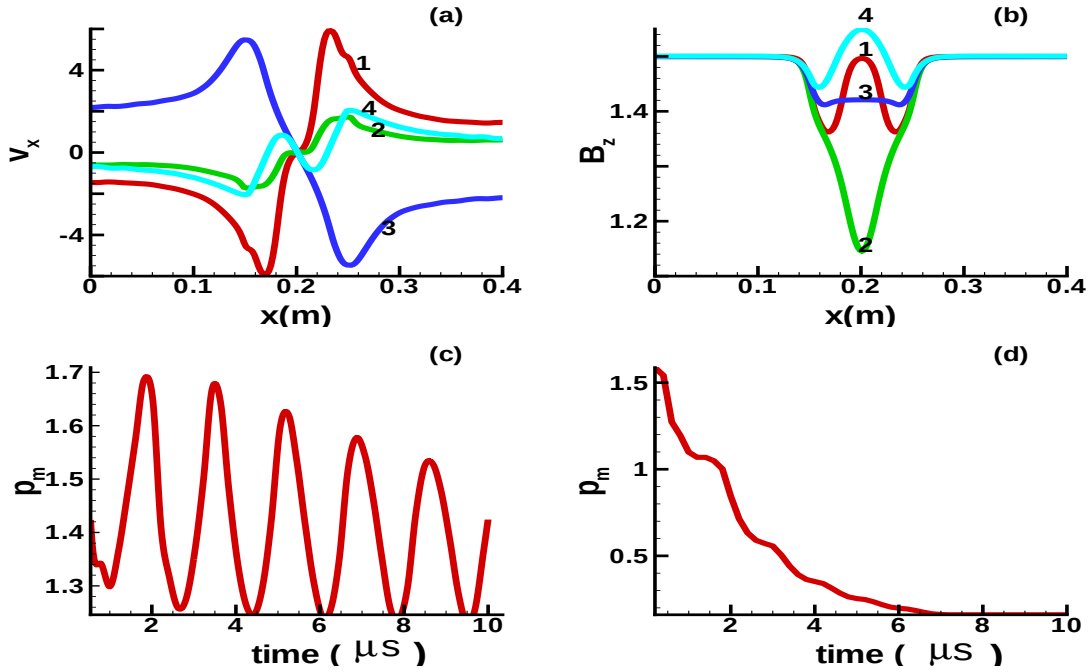

Figure 3. Expansion of a high-pressure cylindrical plasma blob placed at the centre of the poloidal computational domain: (a) plasma velocity ($10^3 m/s$), (b) magnetic field strength B_z ($Tesla$); (c) the pressure maximum ($10^5 N/m^2$) monitored in the poloidal plane as a function of time with toroidal outflow velocity set equal to zero, (d) pressure maximum ($10^5 N/m^2$) with toroidal outflow velocity limited to sonic velocity. The four curves correspond to time instants of 0.4, 0.8 1.4, and 1.8 μs, respectively.

Note that in these shock wave tests the initial plasma parameters on both sides of the shock waves (temperature, density) were chosen and combined in an arbitrary manner. In realistic pellet situations, these quantities are not independent of each other. Obviously, the relevance of shock effects can only be assessed by means of models in which the ablation rate is computed as a function of the plasma state parameters in a self-consistent manner. For the ablation rate - plasma temperature combinations prevailing in up-to-date confinement machines, pellet-caused shock heating seems to be ignorable. Computations under reactor conditions are still to be done.

4.2. Stationary Particle Source

As next step, a stationary particle source of given strength ($\dot{S}_{abl} = 4 \times 10^{23} s^{-1}$) and size (diam.= 4 mm) was placed in the center of the mesh system (x=y=0.20 m). The neutral particles fed to the plasma were assumed to be of room temperature. At time = 0 the source was turned on and its strength was kept constant thereafter. In this run, the toroidal outflow velocity was set equal to zero.

The plasma and pellet input parameters used in this scenario are as follows:
$n_{e0} = 10^{20} m^{-3},\ T_0 = 500\ eV,\ B = 1.5\ Tesla,\ T_{pel} = 270\ K.$

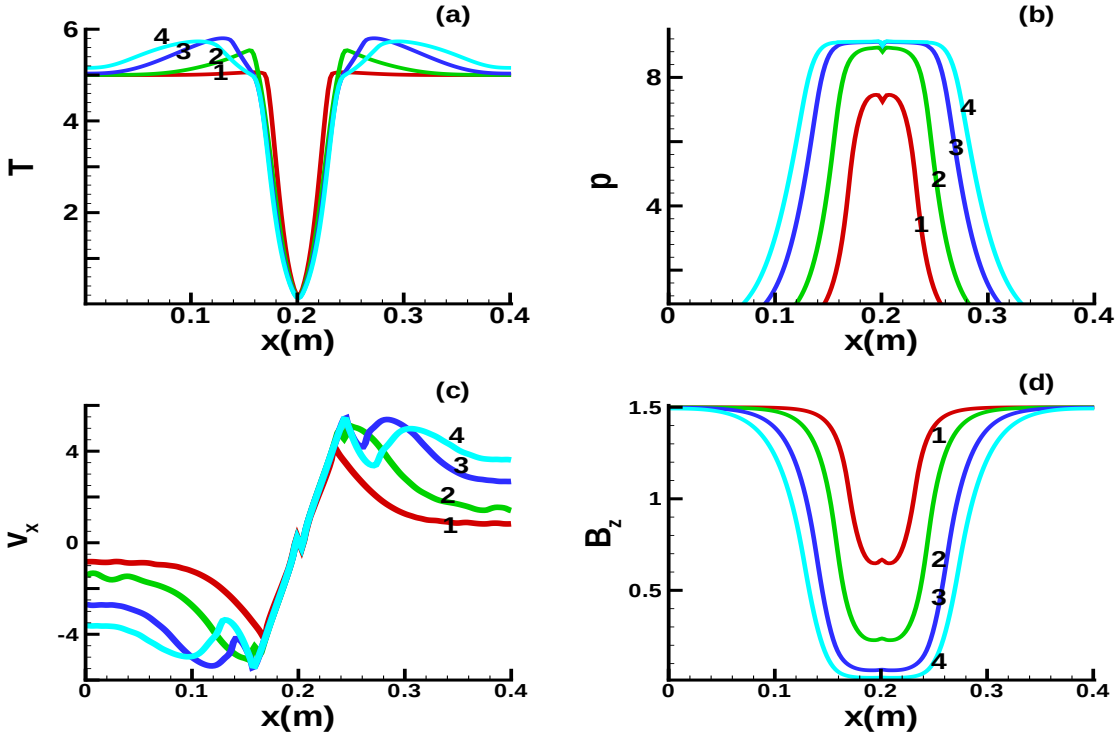

Figure 4. Plasma parameter variations in the poloidal plane when a stationary particle source of $r_{pel} = 2\ mm$ size and $\dot{S}_{abl} = 4 \times 10^{23}\ s^{-1}$ strength is placed at the centre of the computational domain (x=y=0.20m). (a) temperature ($10^2 eV$), (b) pressure ($10^5 N/m^2$), (c) velocity ($10^3 m/s$), (d) magnetic field strength B_z ($Tesla$). The four curves correspond to time instants of 5, 10, 15 and 20 μs, respectively.

Figures 4a to 4d show the evolutions of the (a) temperature, (b) pressure, (c) velocity, and (d) magnetic field distributions along the pellet path in the central plane (y = 0.20 m).

The four curves appearing in each figure correspond to time levels of 5, 10, 15, and 20 μs, respectively.

Similarly to the cases already discussed, the neutral cloud first expands in a cylindrically symmetric manner, becomes heated and ionized. Once ionization sets in, the ablatant interacts with the magnetic field and, similarly to the previous case, a diamagnetic cavity

forms around the particle source. The confinement radius is in this case approximately 4 cm.

This value is consistent with confinement radii (computed and/or measured) reported in previous publication (see, for example, [7] or [9]). The actual confinement radius value depends, of course, upon the prevailing or specified physical conditions.

The central density increases over three orders of magnitude within the first 20 μs. Accordingly, a 'deep hole' develops in the temperature profile: the local temperature drops from 500 eV to about 5 eV (Fig. 4a). At the same time, a temperature wave with an amplitude of about 15% of T_{e0} is propagating into the background plasma. The wave amplitude is a function of the $\chi_{e\perp}$ value specified: 1 m^2/s was used in these calculations. Due to intense cooling at the pellet location, a local dip appears at the center of the pressure distribution curve (Fig. 4b). As a result of this locally reversed pressure profile, velocity reversal takes place in the neighbourhood of the particle source (Fig. 4c), mass being transported towards the center. Owing to the attachment of the magnetic field to the plasma mass (quasi-frozen-in conditions), a hump appears at the center of the magnetic field distribution (Fig. 4d). This hump may become amplified or it may disappear with time, depending upon the initial conditions and transport coefficients specified. The magnitude of this pressure reversal depends upon the combination of the input parameters specified ($\dot{S}_{abl}$, T_0, and $\chi_{e\perp}$ in particular). At low outflow velocities, pressure reversal at the pellet location is usually the case. Note also the developing local maxima/minima in the velocity distribution curve at the edge (periphery) of the temperature valley. These disturbances are caused by the maxima of the magnetic field gradient and the associated $\mathbf{j} \times \mathbf{B}$ force values acting at this radius.

As has been shown in the previous section (4.2), if toroidal expansion is present and the ablated substance may escape along the field lines, the probability of transverse oscillations is drastically reduced, though not completely eliminated (see the magnetospheric barium cloud experiments cited above). The presence or absence of transverse oscillations is likely a function of the relaxation times associated with pressure increase at and mass removal from the locus of particle source.

Hence the flow reversal seen in Fig. 4, the dip in the pressure curve, and the hump at the center of the magnetic field curve may become weakened or completely disappear, depending upon the magnitude of the outflow velocity. Once more, an accurate determination of the toroidal expansion characteristics is warranted.

5. Particle Sources Traversing the x,y Plane

In these scenarios, particle sources of given strengths were injected in the poloidal plane parallel to the x-axis. The translational velocity of the source was chosen between 750 and 1500 m/s and was kept constant during each scenario.

5.1. Single Particle Source

Figure 5a to 5d correspond to a case with the following recipient plasma and particle source parameters (see also section 4.2):

$n_{e0} = 10^{20} m^{-3},\ T_0 = 500eV,\ B = 1.5Tesla,\ T_{pel} = 270\ K,$
$\dot{S}_{abl} = 4 \times 10^{23} s^{-1},\ v_{pel} = 1500 m/s.$ The anomalous electron thermal conductivity value assumed here is, as before, $\chi_{e\perp} = 1\ m^2/s.$

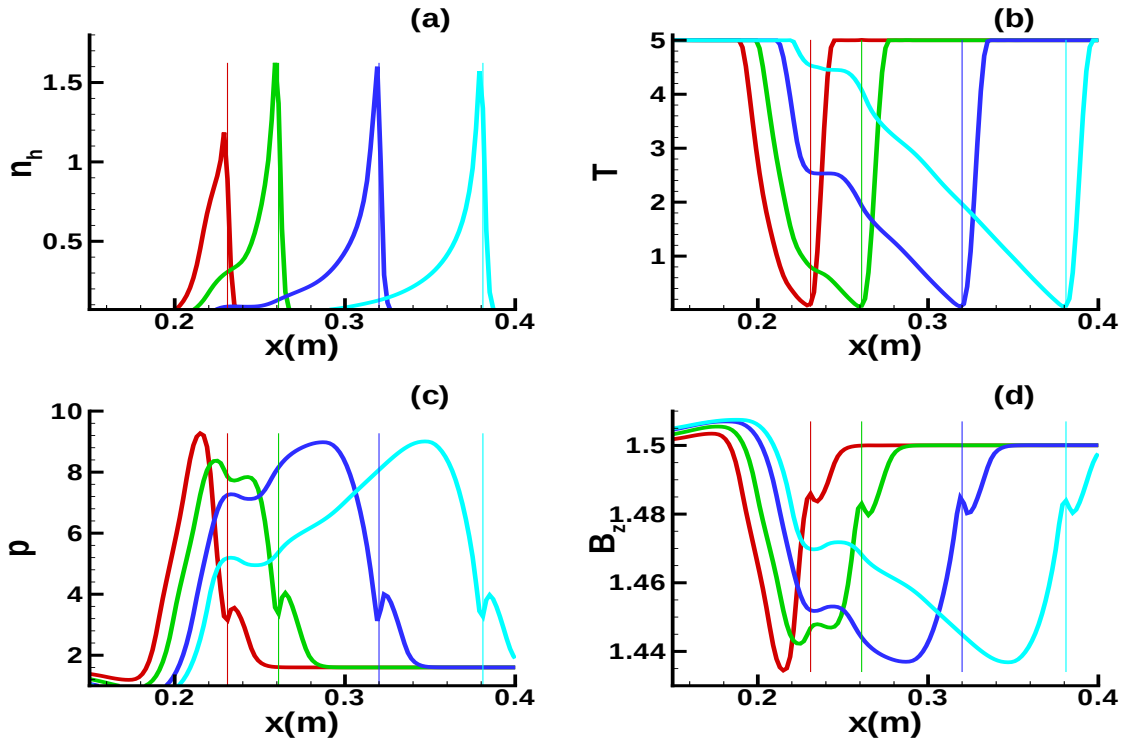

Figure 5. Spatial and temporal variations of the plasma parameters in the poloidal plane when a single particle source of $\dot{S}_{abl} = 4 \times 10^{23}\ s^{-1}$ strength traverses the poloidal plane parallel to the x-axis (y=const=0.20 m). (a) heavy particle density ($10^{22} m^{-3}$), (b) temperature ($10^2 eV$), (c) pressure ($10^4 N/m^2$), (d) magnetic field strength B_z ($Tesla$). The four curves correspond to time instants of 20, 40, 80, and 120 μs, respectively.

The pellet traverses the poloidal plane parallel to the x-axis (y = 0.20 m). The computed toroidal velocities are sonic-limited. Displayed are the (a) density-, (b) temperature-, (c) pressure-, and (d) the magnetic field strength distributions along the pellet path. The gas is practically fully ionized. The four curves shown in each figure correspond to the time levels 20, 40, 80, and 120 μs, respectively. The momentary pellet positions are marked by thin (vertical) lines. Note the dip in the pressure- and the hump in the magnetic field distributions at the momentary pellet locations. The cause of these local disturbances was discussed in the previous section. Local velocity reversal may take place also in this case.

For the same scenario, the two-dimensional distributions of the temperature,

density, pressure, and magnetic field at t = 120 μs are given in the colour contour plots Figures 6a to 6d, respectively. In these plots, the initial and the momentary positions of the particle source are marked by circles. The shape of the partially ionized fraction of the the plasma in the core of the wake closely resembles experimentally observed radiation patterns (see, for example, Fig. 2 of [9]). The width of the wake at any position is approximately twice of the local ionization radius.

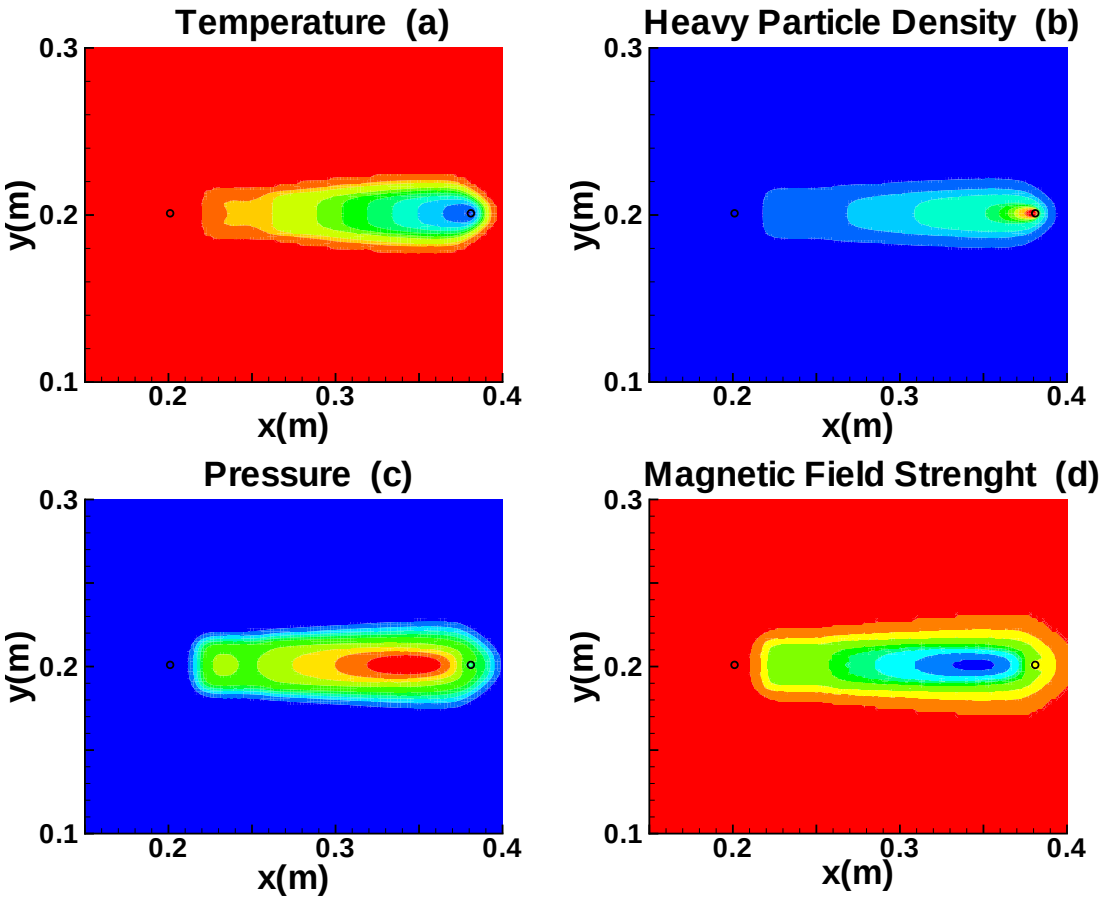

Figure 6. Two-dimensional contour plots of the plasma parameter distributions displayed in Figure 5 for t = 120 μs. The initial and momentary positions of the particle source are marked by black circles. (a) temperature (colour scale 10 to 500 eV), (b) heavy particle density (colour scale 2 to 100 times $10^{20} m^{-3}$), (c) pressure (colour scale 2 to 8 times $10^4 N/m^2$), (d) magnetic field strength B_z (colour scale 1.44 to 1.50 $Tesla$). An anomalous thermal conductivity value of $\chi_{e\perp} = 1\ m^2/s$ was used in the computations.

Notable is the qualitative difference between the density plot and the plots representing the pressure and magnetic field distributions. While the location of the density maximum practically always coincides with the momentary particle source location, the pressure maximum and the magnetic field minimum lag in this case behind the pellet position.

These distributions are strongly affected by the thermal transport processes taking

place in the plasma. If the effective value of the anomalous thermal conductivity acting in the B-perp direction is increased by two orders of magnitude, different patterns result: the minima/maxima of all plasma parameters move closer to or coincide with the respective pellet locations.
Figures 7a and 7b are pressure- and magnetic field contour plots that correspond to Figs. 6b and 6c, respectively, but computed with an assumed anomalous thermal conductivity of 400 m^2/s. The locations of the computed minima/maxima practically coincide with the pellet location.

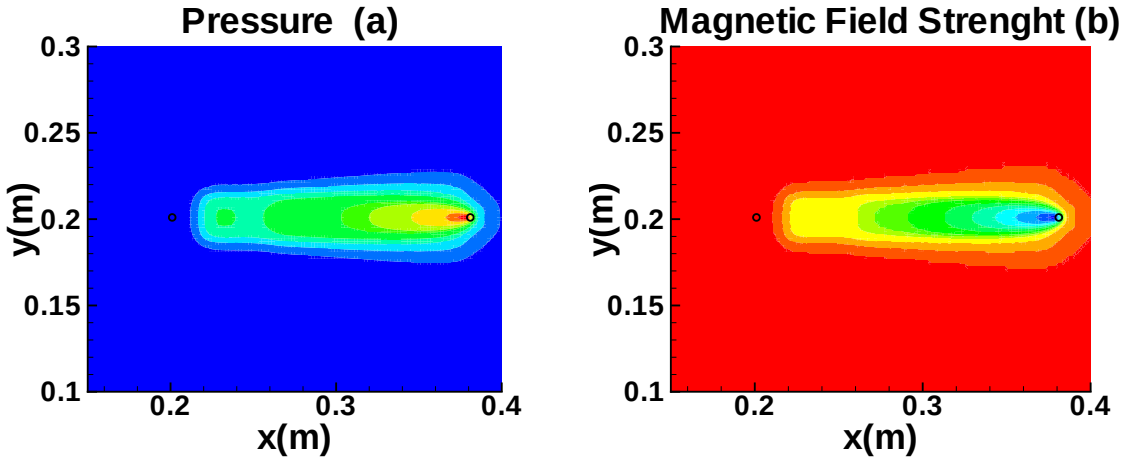

Figure 7. Two-dimensional contour plots of the pressure and magnetic field distributions shown in Figure 6 computed with an anomalous thermal conductivity value of $\chi_{e\perp} = 400\ m^2/s$. (a) pressure (colour scale 0.2 to 1.3 $10^5 N/m^2$), (b) magnetic field strength B_z (colour scale 1.40 to 1.50 $Tesla$).

Some previous calculations [27] had shown that, in order to reproduce experimentally observed radiation patterns in deuterium pellet plasmas, e.g. the lengths of the radiating filaments along the magnetic field lines, the heat transport in the B-perp direction must be increased by a factor of about 400 compared to the case of classical conduction with a 'standard' anomalous diffusivity of 1 m^2/s. Apparently, the same can be concluded on the basis of the present results. Only the magnitude of the necessary heat input is estimated here, without information on the true nature of the transfer processes involved [27]. Since the plasma-cloud interface is subject to Rayleigh-Taylor instability, turbulent mass mixing may also play a role here.

The shift of the pressure maximum with respect to the pellet location computed as a function of the thermal fluxes acting in the B-perp direction may have practical applications. Comparing the magnitude of this computational shift (of about 3 cm in the given case) with results of experimental temperature and density profile measurements in the pellet wake may yield information on the magnitude of the effective heat fluxes, or the value of the anomalous thermal conductivity, acting in the B-perp direction in pellet-fuelled plasmas.

5.2. Two Pellets Injected Simultaneously

In this scenario, two particle sources were launched in the poloidal plane parallel to the x-axis in anti-parallel directions.

The field and source parameters used in this 'gazing meteorite' scenario are as follows: $T_{e0} = 0.5\ keV$, $n_{e0} = 10^{20}\ m^{-3}$, $B = 1.5\ Tesla$, $r_{pel} = 2\ mm$, $v_{pel} = 1500\ m/s$ (launching coordinates 0.26,0.19) and $v_{pel} = -1500\ m/s$ (launching coordinates 0.34,0.21), $\dot{S}_{abl} = 4 \times 10^{23} s^{-1}$ for both pellets.

Of interest are in these almost-colliding-pellet scenarios the maxima of temperature and density values that can be obtained in the disturbed region.

Figure 8a and 8b show the structure of the cloud temperature distributions for two time instants: first, during the approach phase (t = 21.6 μs), and second, after the two sources have passed each other (t = 36.1μs). The interference of the two clouds is apparent.

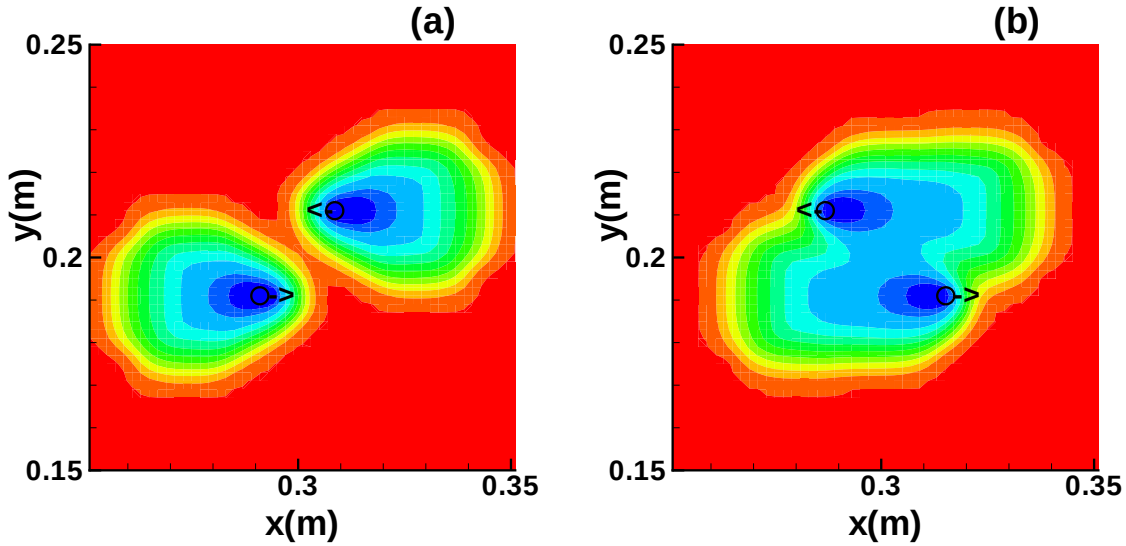

Figure 8. Two-dimensional contour plots of the temperature distribution for the case of two mass sources traversing simultaneously the poloidal computational domain in anti-parallel directions. Colour scale: 30 to 500 eV; (a) time = 21.6 μs, (b) time = 36.1 μs.

Since the possibility of solid-solid interaction is not included into the present physical model, the case of colliding pellets was not considered, and no attempt was made to optimize the relative position of the pellet trajectories nor the angle between the injection directions.

The eventual gain in the temperature- and density maxima can be correctly estimated only if the source-source interaction, the ablation, and the anomalous thermal transport processes are calculated in a self-consistent way. Once these sources of uncertainty are overcome, some interesting pellet scenarios may become subject to consideration.

For example, the possibility of pellet-injection-triggered density ramp-up and ignition

of a low-density over-heated plasma was considered some time ago (see, for example, [28]). The applicability of this method, if workable at all, cannot be checked without self-consistent pellet codes attached to reliable transport calculations. The values of the transport coefficients assumed play a crucial role also in this case.

6. Summary and Conclusions

— The quasi-three-dimensional code consisting of a two-dimensional resistive MHD model for the poloidal plane and a simplified one-dimensional Lagrangian routine for the toroidal direction is found to work reliably. In particular, the code reproduces, with sufficient accuracy, the generalized analytical MHD shock wave relations presented in this work.

— The axially symmetric distributions obtained for cylindrical shocks and stationary particle source scenarios strongly depend upon the set of initial values prescribed, on the particle source strength - background plasma parameter combinations in particular.

— The two-dimensional distributions obtained for a single particle source traversing the plasma produce optical radiation patterns closely resembling those seen in deuterium plasmas with D_2 pellets injected (see, for example, [3]).
The comparison of the computed plasma parameter profiles with measured distributions offers a convenient way for obtaining information on the magnitude of the effective value of the thermal diffusivity $(\chi_{e\perp})_{eff}$ acting in the poloidal plane.

— The two-dimensional computations applied to two particle sources injected simultaneously in the poloidal plane along anti-parallel rays show the versatility of the possible code applications (density ramp-up, shock-heating, etc.).

— The preliminary results reported were obtained with prescribed particle source strengths and a simplified model describing the expansion dynamics in the third (toroidal) dimension. The results show that both of these assumptions have a crucial effect on the results obtained. Hence a reliable analysis of the pellet - plasma interaction process makes the self-consistent determination of the source strength representing the local ablation rate, the accurate computation of the plasma processes taking place in the toroidal direction, and the proper selection of the effective transport coefficients mandatory.

Acknowledgments

Thanks are due to Peter Lang and Hans-Peter Zehrfeld of Max-Planck-Institute of Plasma Physics at Garching for useful discussions.

[1] Parks P B and Turnbull R J 1978 *Phys. Fluids* **21** 1735
[2] Milora S L and Foster C A 1978 *IEEE Trans. Plasma Sci.* **PS-6** 578
[3] Milora S L, Houlberg S L, et al 1995 *Nucl. Fusion* **35** *Sect. 4.2* 657
[4] Kuteev B V, Umov A P, et al 1985 *Sov. J. Plasma Phys.* **11** 236
[5] Houlberg W A, Milora S L, et al 1988 *Nucl. Fusion* **28** 595
[6] Kaufmann M, Lackner K, et al 1986 *Nucl. Fusion* **26** 171
[7] Lengyel L L and Spathis P N 1994 *Nucl. Fusion* **34** 675
[8] Pégourié B and Pichiotino J-M 1993 *Nucl. Fusion* **33** 591
[9] Lengyel L L, Büchl K, et al 1999 *Nucl. Fusion* **39** 791
[10] Pegourie B *Plasma Phys. Contr. Fusion* **49** 87
[11] Lengyel L L 1977 *Nucl. Fusion* **17** 805
[12] Rozhansky V A, Veselova I Yu, et al 1995 *Plasma Phys. Contr. Fusion* **37** 399
[13] Baylor L R, Jernigan T C, et al 1998 *ANS Fusion Techn.* **34** 425
[14] Parks P B, Baylor R L, et al 2000 *Phys. Plasmas* **7** 1968
[15] Müller H W, Dux R, et al 2002 *Nucl. Fusion* **42** 301
[16] Lengyel L L, Rozhansky V A, et al 1997 *Nucl. Fusion* **37** 1245
[17] Borovsky J E 1998 *Phys. Plasmas* **5** 3195
[18] Lengyel L L 1969 *Phys. Letters* **29A** 60
[19] Lalousis P J, Lengyel L L, 2000 *Nucl. Fusion* **40** 1511
[20] Lalousis P J 2006 *Proc. 33rd EPS Conf. on Pl. Physics, ROME ECA* **30I** P-5.173
[21] Kristof G and Lengyel L L 1998 *Phys. Plasmas* **5** 315
[22] R.J. Leveque 2002 *Finite Volume Methods for Hyperbolic Problems* (Cambridge University Press, London)
[23] Saad Y, Schultz M, et al 1985 *J. Sci. Stat. Comput.* **7** 856
[24] Lengyel L L 1978 *Phys. Fluids* **21** 1945
[25] John J E A 1984 *Gas Dynamics* (Second Edition, Allyn and Bacon, Inc., Boston London Sydney Toronto)
[26] Lengyel L L 1988 *Phys. Fluids* **31** 1577
[27] Lalousis P, Lengyel L L, Schneider R 2007 *Proc. 34th EPS Conf. on Pl. Physics, WARSAW* P4.097
[28] Borras K and Lengyel L L 1985 *Amer. Nucl. Soc. 6th Topical Meeting on the Technology of Fusion Energy, S.F., Ca.* Paper 6D-2/12